PHYSICAL REVIEW B VOLUME 51, NUMBER 7 15 FEBRUARY 1995-I

$Al_xGa_{1-x}As$ intervalley scattering rates from field-assisted photoemission spectroscopy

T. R. Parker and C. C. Phillips
Physics Department, Imperial College, London SW7 2AZ, United Kingdom

P. G. May
Sharp Laboratories of Europe Ltd., Edmund Halley Road, Oxford Science Park, Oxford OX4 4GA, United Kingdom

(Received 28 September 1994)

Field-assisted photoemission has been observed from a semiconductor heterostructure with a GaAs-$Al_{0.25}Ga_{0.75}As$ emitter layer and has yielded spectroscopic information on hot-electron energy distributions in the low-electron-density limit. Energy-distribution curves of electrons photoemitted from the structure under high electric fields have been measured as a function of electric field and photon energy. Computer-modeled values for the $Al_xGa_{1-x}As$ intervalley coupling constants have been deduced as follows: $D_{\Gamma L}=(0.30\pm0.10)\times10^9$ eV cm^{-1}, $D_{LL}=(0.70\pm0.10)\times10^9$ eV cm^{-1}, $D_{XX}=(0.70\pm0.05)\times10^9$ eV cm^{-1}, $D_{LX}=(0.70\pm0.15)\times10^9$ eV cm^{-1}, and $D_{\Gamma X}=(1.0\pm0.2)\times10^9$ eV cm^{-1}.

I. INTRODUCTION

In a recent review,[1] methods for determining the intervalley-coupling constants in GaAs were broadly categorized into (a) transport methods that typically model velocity-field characteristics in lightly doped samples and (b) more recent time-resolved optical methods that provide spectroscopic data on hot-electron and phonon distributions under conditions of high (10^{18}–10^{19} cm^{-3}) electron density. The former approach generates data that are compatible with a weak-intervalley-coupling model ($D_{\Gamma L}\approx2\times10^8$ eV cm^{-1}), but are only weakly sensitive to the intervalley-coupling constants and may be susceptible to the effects of electron trapping at impurity states associated with the higher L and X valleys. The latter approach provides higher quality data, but may be susceptible to the effects of spurious additional scattering channels (e.g., plasmon, plasmon-LO phonon, hot-phonon, and electron-hole mechanisms) and has resulted in published intervalley-coupling constants ($D_{\Gamma L}\approx7-10\times10^8$ eV cm^{-1}) almost three times larger than those from the transport studies.

Here we adopt another approach to this problem and exploit the alloy and dopant profile control provided by modern epitaxial growth techniques to produce a heterostructure sample in which the electron energy distributions, in the low-carrier-density limit, can be measured directly. Modeling these electron-energy-distribution curves (EDC's) proves to be a sensitive test of these intervalley-coupling constants and yields significantly improved values.

II. EXPERIMENTAL DETAILS

The sample used (Fig. 1) was initially designed to provide a gatable photoemission current[2] with the lowest possible gating voltage. It was grown by metal-organic chemical vapor deposition and had a lightly p-doped ($N_A=4\times10^{15}$ cm^{-3}) emitter layer with a composition graded parabolically from GaAs to $Al_{0.25}Ga_{0.75}As$ and a highly p-doped (1×10^{19} cm^{-3}) absorber layer. Under zero applied bias, electrons photoexcited in the absorber layer have insufficient energy to surmount the resulting potential barrier in the emitter layer and are not photoemitted [Fig. 1(a)]. Under bias, the small applied voltage appears wholly across the emitter layer, allowing it to

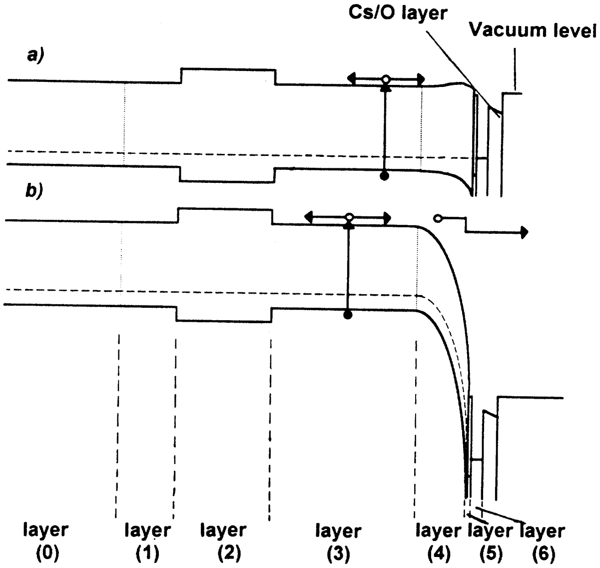

FIG. 1. Schematic of band structure of field-assisted photoemitter heterostructure with (a) zero applied bias, (b) $V_{app}\approx-4$ V. The layer parameters are as follows: layer 0, GaAs substrate, $p\approx5\times10^{18}$ cm^{-3}, 500 μm thick; layer 1, GaAs buffer layer, $p\approx5\times10^{18}$ cm^{-3}, 0.5 μm thick; layer 2, $Al_{0.4}Ga_{0.6}As$ etch stop layer (for transmission mode experiments not reported here), $p\approx5\times10^{18}$ cm^{-3}, 2.0 μm thick; layer 3, GaAs absorber layer, $p\approx1\times10^{19}$ cm^{-3}, 3 μm thick; layer 4, $Al_xGa_{1-x}As$ emitter layer, parabolically graded in composition between $x=0$ and 0.25, $p\approx6\times10^{15}$ cm^{-3}, 0.8 μm thick; layer 5, GaAs capping layer (to avoid surface oxidation in air), $p\approx4\times10^{15}$ cm^{-3}, 5 nm thick; layer 6, Au Schottky contact, 18 nm thick.

0163-1829/95/51(7)/4264(8)/$06.00 51

be fully depleted and removing the potential barrier to photoemission [Fig. 1(b)]. The electric-field distribution in the emitter layer was calculated (see Sec. 2 of the Appendix) from the known dopant profile taken from the diode reverse bias capacitance-voltage (C-V) characteristic. The peak electric field (occurring at the sample surface) varied in the range $E_{\text{surf}} \approx 2-11 \times 10^6$ V m^{-1}.

To allow vacuum photoemission of the photoelectrons, the potential step at the sample surface was removed by activating the gold Schottky contact layer with an overlayer of cesium and oxygen to lower its work function in the manner commonly used to form negative electron affinity photocathodes.[3] Typically this resulted in a vacuum level energy (measured by calibrating the electron spectrometer energy scale and calculating the Schottky barrier height from the device I-V characteristic), which lay ≈ 0.1 eV below the $Al_{0.25}Ga_{0.75}$ As conduction-band edge at the sample surface.[4] External bias voltages were applied between the thin (≈ 18 nm), large-area (13 mm^2) gold Schottky contact at the front of the sample and an Ohmic (Au/Zn) contact at the back of the sample. Reverse biases up to 7 V were attainable with low (less than 8 A m^{-2}) leakage currents.

Samples were solvent cleaned before the Schottky contacts were evaporated in a standard vacuum coating plant at 1×10^{-5} Torr. They were then transferred in air to an UHV ($p = 5 \times 10^{-11}$ Torr) electron spectroscopy system for the photoemission experiments. Immediately prior to sample activation they were ion bombardment cleaned with 100-eV Ar^+ ions at 4 mA m^{-2} until oxygen and carbon contamination peaks were lowered to below the Auger detection threshold of the system.

The EDC's were obtained with ≈ 10 μW of illumination (at $\lambda_{\text{pump}} = 850$, 800, 750, 700, and 650 nm) from a quartz lamp/monochromator and were acquired with a 150° hemispherical electrostatic electron energy spectrometer (originally designed for Auger and x-ray-photoelectron spectroscopy). The sample surface was held at a constant potential (≈ -40 V) relative to the spectrometer to ensure an energy-independent electron collection efficiency as the device bias was varied. Under the biasing conditions used with the spectrometer it had an energy resolution of ≈ 110 meV.[4]

III. RESULTS

A. Qualitative remarks

Figure 2 shows a typical set of EDC's taken at a fixed photon wavelength λ_{pump}, but at various reverse biases. Two experimental artifacts (labeled **a** and **b**) are present and have to be taken into account to isolate the portion of the photoemitted spectrum originating in the semiconductor part of the sample. Feature **a** is due to photoelectrons originating in the gold Schottky contact overlayer; its shape, position, and intensity is independent of sample bias, but dependent on the pump photon energy. Although useful for absolute calibration of the spectrometer energy scale and for checking that the in-plane Ohmic voltage drops across the front contact are negligible, at shorter λ_{pump} values this feature increases in energy width and intensity. Even when subtracted off there is risk of it distorting the shape of the low-energy portion of the semiconductor EDC data and the detailed numerical fitting was therefore confined to the lower photon energy EDC's where the semiconductor photoemission dominated. The feature **b** arises from stray light causing photoemission from the metal sample holder (connected to the rear of the sample), which also becomes cesiated during the activation process; it moves linearly with applied bias and has a negligible effect on the semiconductor EDC shape for reverse bias voltages > 0.3 V.

For biases > 0.6 V the semiconductor photoemission peak increases in width approximately linearly at a rate of ≈ 0.1 eV per volt of bias. The energy of the maximum of the semiconductor peak also varies approximately linearly (at a rate of ≈ 0.08 eV per volt of bias) for $-0.6 > V_{\text{app}} > \approx -4.5$ V. $V_{\text{app}} = -4.5$ V corresponds to a mean and peak electric field in the emitter layer of 5.5

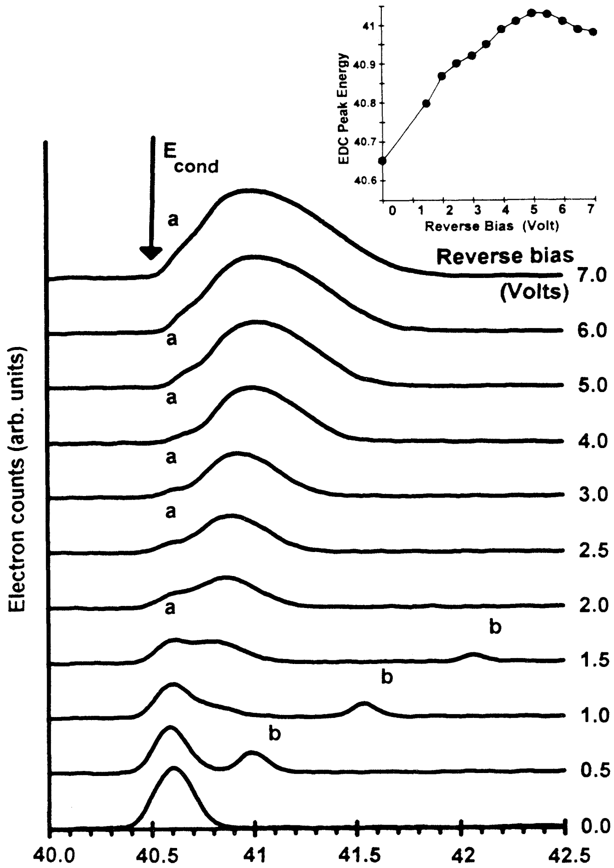

FIG. 2. Measured EDC's from the sample at various reverse bias voltages under $\lambda_{\text{pump}} = 850$ nm illumination in the reflection mode. Peaks marked **a** and **b** are spurious signals arising from the Schottky contact and the sample holder, respectively (see text). On this scale the $Al_{0.25}Ga_{0.75}As$ conduction-band minimum at the sample surface corresponds to a measured electron energy (E_{cond}) of 40.48 eV. Inset: bias dependence of the energy of the peak of the EDC under these experimental conditions.

and 8.2×10^6 V m^{-1}, respectively, and at this bias the peak in the semiconductor EDC corresponds to an electron energy ≈ 0.53 eV above the $Al_{0.25}Ga_{0.75}As$ conduction-band edge at the sample surface.

At higher biases, however, the increase in EDC peak energy with bias slows markedly (Fig. 2 inset) for reasons that are at present uncertain. One possibility is that, at these very high fields, an efficient scattering mechanism becomes available to electrons with energies $> \approx 0.53$ eV above the conduction-band minimum.

In GaAs the published energy difference between the X_{6c} and X_{7c} conduction-band minima is 0.35 eV.[5] Although accurate estimates are currently unavailable for $Al_xGa_{1-x}As$, the mean Al concentration in the emitter layer is only 8% and if the X_{6c}-X_{7c} energy splitting is assumed to be the same in the alloy, then the $Al_{0.25}Ga_{0.75}As$ X_{7c} minimum lies ≈ 0.55 eV above the conduction-band edge at the sample surface. The onset of intervalley scattering into this second conduction-band valley could therefore be the origin of the slowing of the field heating of the electron distribution with increasing bias, although, as the effective mass in the X_{7c} valley is estimated to be only moderately large [$\approx 0.48 m_0$ (Ref. 6)], rather large intervalley coupling constants to the X_{7c} valley would be required to explain the data quantitatively.

B. Quantitative modeling

In order to extract quantitative values for the intervalley-coupling constants, a Monte Carlo scheme was used to generate modeled semiconductor EDC's for comparison with the experimental data. The doping and alloy composition variations in the sample as a function of distance d from its surface were used in a Poisson analysis to calculate the potential distributions and effective fields in the Γ, L, and X valleys as a function of applied bias using the materials parameters of Table I.

The photoelectron generation rate profiles $G(d)$ were calculated as a function of λ_{pump} by using a position-dependent absorption coefficient spectrum calculated from the GaAs optical absorption coefficient spectrum shifted rigidly upward in photon energy by the increase in band gap with aluminum concentration x. The electron scattering processes were then modeled (using the materials parameters of Table I) as follows.

(i) Starting at the sample surface ($d=0$), an electron was placed in the Γ valley at a distance d and was given an initial energy of $A(h\nu-E_g)$, where $A = m_{hh}^*/(m_{hh}^*+m_c^*) \approx 0.9$[7] and a mean initial momentum of zero.

(ii) Over a suitably small time interval Δt, the probabilities of the various scattering mechanisms were then calculated (using the materials parameters appropriate to the alloy composition at that position in the sample) and a random number was generated to determine which (if any) scattering process occurred in that interval. The energy, the momentum, and the valley of the electron were changed accordingly.

(iii) The valley-dependent energy and momentum gain of the electron from the electric field and the distance traveled in the interval Δt were calculated.

(iv) Steps (ii) and (iii) were repeated until the electron reached the surface. The energy E and the valley i of the electron were then recorded. The EDC for that valley was incremented with a contribution at the energy E and weighted by $G(d)$.

(v) The initial depth d of the photoexcited electron was incremented and steps (i)–(iv) were repeated until d was large enough for the number of electrons photoexcited at d and being photoemitted to be negligible.

(vi) Steps (i)–(v) were repeated to generate modeled EDC's with adequate statistics. EDC's for the Γ, L, and X valleys were stored separately and were added (with appropriate weighting to simulate the valley-dependent sur-

TABLE I. Values of the material parameters used in the model.

Parameter	Value	Units	Equation number	Reference
$Al_xGa_{1-x}As$ alloy variation with depth	$x=1\times10^{12}(L_d-d)^2$		(31)	
Density	$\rho=5360-(1600x)$	kg m^{-3}	(32)	7
Intravalley phonon enegy	$E_{p0}=36.25+1.83x+17.12x^2-5.11x^3$	meV	(33)	7
Intravalley phonon energy	$E_{ij}=0.8E_{p0}$	meV	(34)	7
Band gap	$E_g=1.424+1.247x$	eV	(35)	7
L-valley band gap	$E_{gL}=1.708+0.642x$	eV	(36)	7
X-valley band gap	$E_{gX}=1.90+0.125x+0.143x^2$	eV	(37)	7
Γ-band-edge effective mass	$m_\Gamma^*=0.067+0.083x$	m_0	(38)	7
L-valley density-of-states mass	$m_{DOS}^L=0.56+0.1x$	m_0	(39)	7
X-valley density-of-states mass	$m_{DOS}^X=0.85-0.14x$	m_0	(40)	7
L-valley conductivity mass	$m_c^L=0.11+0.03x$	m_0	(41)	7
X-valley conductivity mass	$m_c^X=0.32-0.06x$	m_0	(42)	7
Static dielectric constant	$\epsilon_s=13.18-3.12x$		(43)	7
High-frequency dielectric constant	$\epsilon_\infty=10.89-2.73x$		(44)	7
Effective acoustic deformation potential	$\Xi_{\text{eff}}=6.7-1.2x$	eV	(45)	7
Average elastic constant	$C_L=7.73+0.14x$	10^6 N cm^{-2}	(46)	7
Thickness of lightly doped emitter layer	$L_d=0.8$	μm		
Acceptor density in emitter layer	$N_A=4.2\times10^{15}$	cm^{-3}		
Schottky diode built-in voltage	$V_{bi}=0.52$	V		

face emission probabilities) to generate the final overall calculated EDC.

To improve computational efficiency the following approximations were made.

(a) The diffusion of electrons from the absorber layer to the emitter layer was simulated by assuming that all the photoelectrons that manage to diffuse to the emitter layer reach it with $3/2k_BT$ energy and a mean momentum parallel to the electric field of zero. Detailed scattering calculations were made only within the emitter layer.

(b) An ideally abrupt step in dopant density was assumed at a depth of 0.8 μm from the sample surface (in line with the measured C-V profile). For $d<0.8$ μm the sample was assumed to be doped at $p=4.2\times10^{15}$ cm^{-3}. The absorber layer was assumed to have a sufficiently high doping level for the field within it to be zero for $d>0.8$ μm.

(c) Scattering processes which contributed $<1\%$ to the total scattering rates (Sec. 1 of the Appendix) were neglected. This resulted in the following energy relaxing processes being included: polar LO intravalley scattering, optical-phonon equivalent and nonequivalent intervalley scattering [Eqs. (A1), (A4), (A10), and (A11) in the Appendix]. Nonparabolicity was taken into account for scattering processes involving the Γ valley.

(d) Since, to a good approximation, acoustic-phonon and alloy scattering relax only momentum, they were not included in the detailed calculation of the random scattering events. Rather, a mean degree of momentum relaxation due to acoustic-phonon and alloy scattering was calculated at each Δt and the electron momentum was adjusted accordingly [Eqs. (A13) and (A14) in the Appendix].

Due to the presence of the amorphous gold/cesium-oxygen overlayer, in-plane momentum conservation rules could not be applied with confidence to the surface emission process and it was not possible to calculate the valley-dependent surface emission probabilities with acceptable accuracy. In practice, however, this uncertainty had only a minor effect on the fitting process since the Γ-X and Γ-L splittings in $Al_{0.25}Ga_{0.75}As$ at the sample surface were each smaller than both the spectrometer resolution and the widths of the EDC's in each of the valleys (Fig. 3). The modeled EDC shape was to a good degree independent of the ratios chosen for the surface emission probabilities in each valley and they were therefore all set to be equal.

The values of D_{ij}, the intervalley-coupling constants, were varied (within the range of previously published values) to optimize the fit between the modeled and experimental data sets. Since the intervalley scattering rates (which are generally dominant) are proportional to D_{ij}^2, the shape and size of the modeled EDC's depend critically upon the values of D_{ij} used. As an illustration of the sensitivity of this fitting process, the inset of Fig. 4 shows modeled EDC's calculated with the upper and lower limits of the D_{ij} published by Adachi.[7]

At present, the intervalley-coupling constants for scattering between the first and second conduction bands are unknown and, although published values for the X_{7c}

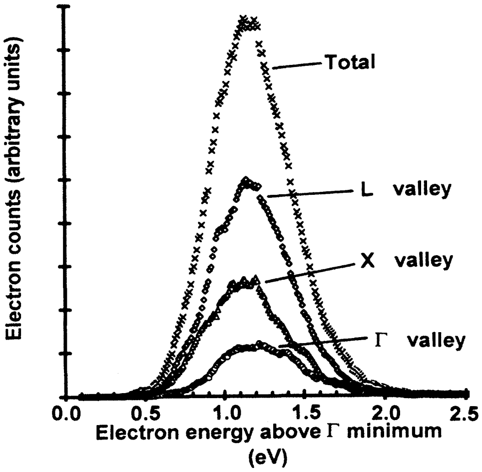

FIG. 3. Calculated EDC's for the individual conduction-band minima for $V_{app}=-7$ V and $\lambda_{pump}=850$ nm using the best-fit coupling constant values of Table II. Total denotes the predicted emitted EDC assuming equal surface emission probabilities for the three valleys.

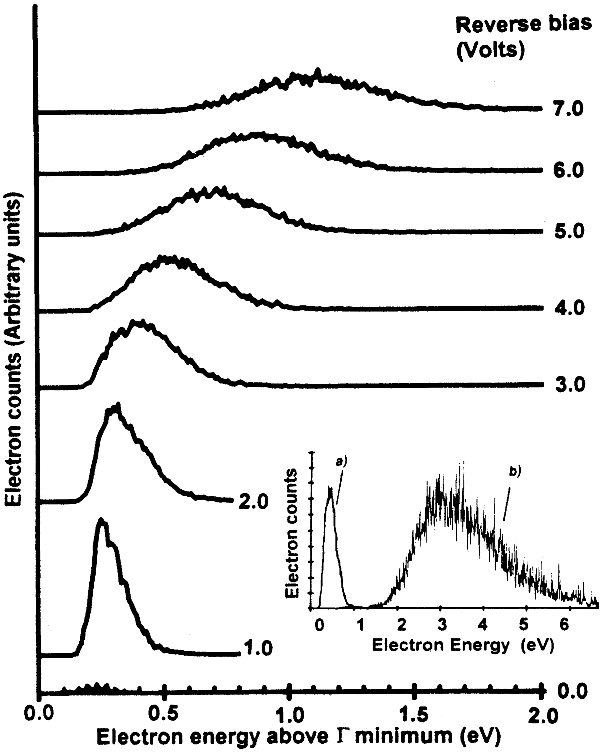

FIG. 4. Modeled EDC's using the best-fit values for the coupling constants of Table II for the experimental conditions appropriate to Fig. 2 and with the surface emission probabilities for electrons in each of the valleys set to be equal. Inset: modeled EDC's for $V_{app}=-7$ V using (a) the maximum ($D_{\Gamma L}=1\times10^9$ eV cm^{-1}, $D_{LL}=1\times10^9$ eV cm^{-1}, $D_{XX}=1.1\times10^9$ eV cm^{-1}, $D_{LX}=1.1\times10^9$ eV cm^{-1}, and $D_{\Gamma X}=1.1\times10^9$ eV cm^{-1}) and (b) the minimum [$D_{\Gamma L}=0.15\times10^9$ eV cm^{-1}, $D_{LL}=1\times10^9$ eV cm^{-1}, $D_{XX}=0.27\times10^9$ eV cm^{-1}, $D_{LX}=0.34\times10^9$ eV cm^{-1}, and $D_{\Gamma X}=0.5\times10^9$ eV cm^{-1}) coupling coefficient values quoted by Adachi (Ref. 7).

TABLE II. Values used in the text.

Coupling constant	$D_{\Gamma L}$ (10^9 eV cm^{-1})	D_{LL} (10^9 eV cm^{-1})	D_{XX} (10^9 eV cm^{-1})	D_{LX} (10^9 eV cm^{-1})	$D_{\Gamma X}$ (10^9 eV cm^{-1})
GaAs published value from Adachi (Ref. 7)	0.15-1.0	1	0.27-1.1	0.34-1.1	0.5-1.1
GaAs published value from Mickevicius and Reklaitis (Ref. 1)	0.18	0.5		0.3	1.0
Best-fit values from this work	0.3±0.1	0.7±0.1	0.7±0.05	0.7±0.15	1.0±0.2

effective mass and X_{6c}-X_{7c} band gap are available for GaAs, we know of no such data for the $Al_xGa_{1-x}As$ alloy. To reduce the number of free fitting parameters it was therefore assumed throughout that the second conduction band did not participate in the transport of photoelectrons to the surface and the fitting process was restricted to data sets (i.e., for reverse biases <4.5 V) where the possible influence of this second band was judged (on the considerations outlined in Sec. III A) to be negligible.

The EDC model calculation was iterated to find the best fit between the modeled and experimental EDC data. The criteria used to define a good fit were when the width and the shape of the modeled EDC most resembled the experimental data and when the modeled EDC spanned the correct energy range. The only practical way of applying these criteria was by eye and each of the D_{ij} values was varied between the limits given by Adachi[7] (Table II) in 0.1×10^9 eV cm^{-1} steps.

IV. DISCUSSION

During the fitting process strong trends in the dependence of the EDC shape and size which were highly sensitive to the assumed values of the D_{ij}'s became immediately apparent. The errors to the best-fit values in Table II were estimated by varying each of the D_{ij}'s in turn around the best-fit values until the visual fit deteriorated noticeably.

A typical modeled EDC data set produced with these values is shown in Fig. 4. At all biases and wavelengths (with the exception of the high-electric-field-heating regime discussed in Sec. III A) the quality and range of the fit, in terms of the variation of high-energy edge, full width at half maximum, and overall shape with applied reverse bias, was similar to that in Fig. 3.

With the exception of D_{LL} (where he quotes only one value 1×10^9 eV cm^{-1}), the deduced D_{ij}'s are within the range of values of D_{ij} quoted by Adachi[7] for GaAs. In their review article on intervalley scattering in GaAs, Mickevicius and Reklaitis[1] argue for coupling constants in GaAs (Table II) differing by a few standard errors from the values deduced from our data here.

The mean aluminum concentration in the emission layer is low (25% maximum, with an average of 8%) and it is not possible to isolate the alloy concentration dependence of the coupling constants in our data. In spite of the uncertainties introduced by the presence of aluminum in our samples, however, we feel that our data strongly support Mickevicius and Reklaitis's[1] arguments in favor of a weak Γ-L coupling model.

Our model treated the transport of electrons through a particular sample, but with minor alterations it could be used to calculate the velocity-field (v-E) characteristics of electrons in bulk GaAs and $Al_xGa_{1-x}As$ for comparison with established experimental v-E data as a test of the accuracy of our model and the scattering factor extracted from it. The modeled v-E data for GaAs are shown in Fig. 5 together with previously published experimental data[8] and the fit is good. Also shown is a v-E characteristic for $Al_{0.25}Ga_{0.75}As$ calculated using the same formalism. Figure 6 summarizes the relative strengths of the various electron scattering rates for

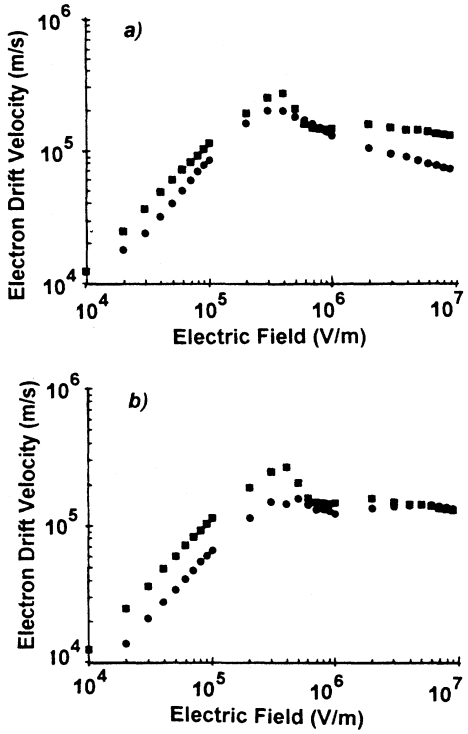

FIG. 5. (a) Velocity-field curves for electrons in GaAs; squares, modeled data using best-fit coupling constant values from this work; circles, experimental data from Ref. 8. (b) Velocity-field curves for electrons in GaAs (squares) and $Al_{0.25}Ga_{0.75}As$ (circles) modeled using best-fit coupling constant values from this work (Table II).

GaAs and $\mathrm{Al}_{0.25}\mathrm{Ga}_{0.75}\mathrm{As}$ using our best-fit coupling constant values.

V. CONCLUDING REMARKS

A way of measuring intervalley-coupling constants has been developed that provides spectroscopic data on hot-electron energy distributions in the $\mathrm{Al}_x\mathrm{Ga}_{1-x}\mathrm{As}$ alloy system in the low-electron-density, high-electric-field regime appropriate to the modeling of high-speed electronic devices. The coupling constant values obtained are in good agreement with the weak Γ-L coupling model based on previously published transport-based data and differ at a very high level of significance from the strong Γ-L coupling values derived recently from high-electron-density time domain optical studies. The coupling constant values derived here have been shown to adequately predict the velocity-field characteristics of bulk GaAs, and tentative evidence for the onset of scattering into the X_{7c} minima in the second conduction band for fields in excess of $\approx 6\times10^6$ V m^{-1} has been presented.

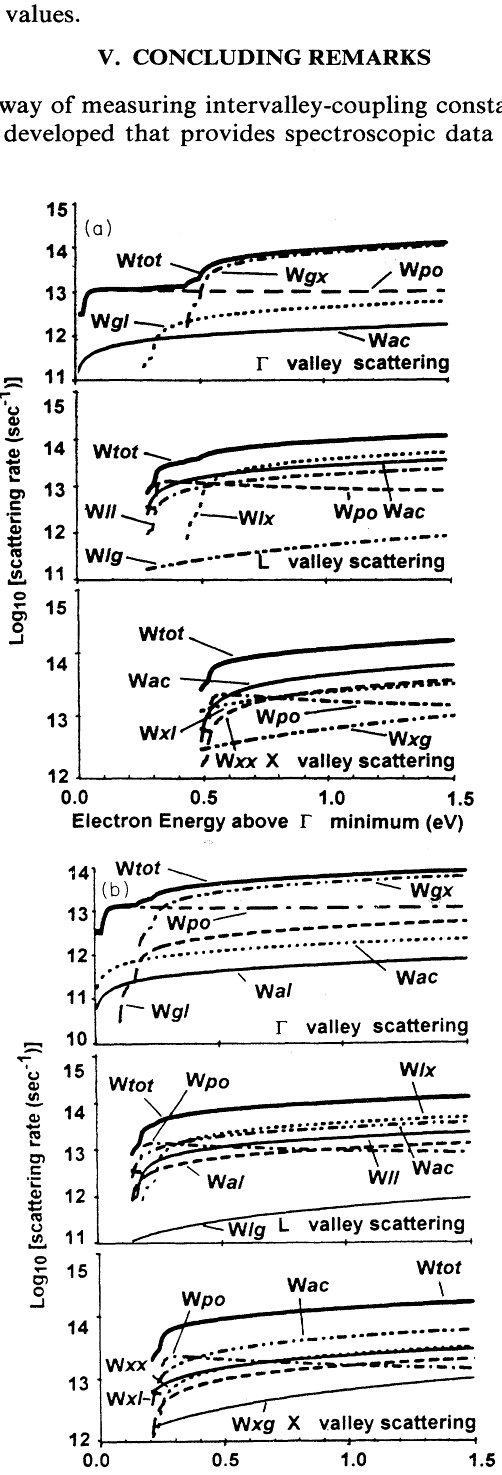

FIG. 6. Summary of scattering rates (sec^{-1}) for the three lowest minima in (a) GaAs and (b) $\mathrm{Al}_{0.25}\mathrm{Ga}_{0.75}\mathrm{As}$ calculated using the best-fit values of Table I. W_{tot}, total scattering rate; W_{p0}, optical-phonon intravalley scattering; W_{gx} W_{gl}, W_{lx}, W_{lg}, W_{xl}, W_{xg}, optical-phonon intervalley scattering between nonequivalent valleys; W_{ac}, acoustic-phonon intravalley scattering; W_{ll}, W_{xx}, optical-phonon equivalent-intervalley scattering.

ACKNOWLEDGMENTS

We would like to acknowledge the help of Sharp Laboratories of Europe Ltd. for financial support and for the supply of MOCVD samples and Delli Delti Ltd. for financial support for T.R.P.

APPENDIX: SCATTERING RATE EQUATIONS AND MATERIAL PARAMETERS USED IN THE EDC MODELING

1. Detailed scattering rate calculations

(a) Intravalley phonon scattering

The polar LO-phonon intravalley scattering rate in the L and X valleys was calculated within the parabolic band approximation as[9]

$$W(\mathbf{k})=\frac{e^2\omega_0 m^{*1/2}}{2\pi\epsilon_p\hbar(2E_k)^{1/2}}\times\left[n(\omega_0)\sinh^{-1}\left[\frac{E_{\mathbf{k}}}{\hbar\omega_0}\right]^{1/2}+\{n(\omega_0)+1\}\sinh^{-1}\left[\frac{E_{\mathbf{k}}}{\hbar\omega_0}-1\right]^{1/2}\right], \tag{A1}$$

where ω_0 is the phonon frequency, ϵ_p is the effective permittivity defined [Eq. (A2)], and $n(\omega_0)$ is the phonon population number [Eq. (3)]

$$\epsilon_p=\epsilon_s\epsilon_\infty/\epsilon_s-\epsilon_\infty\ , \tag{A2}$$

$$n(\omega_0)=\frac{1}{\exp(E_{\mathrm{LO}}/k_BT)-1}\ , \tag{A3}$$

where ϵ_s is the static dielectric constant, ϵ_∞ is the high-frequency dielectric constant, and E_{LO} is the LO phonon energy. The polar LO-phonon intravalley scattering rate in the Γ valley was calculated considering nonparabolicity as[10]

$$W(\mathbf{k})=\frac{e^2\omega_0^2 m^{*1/2}}{4\pi\epsilon_p[2\gamma(E_\mathbf{k})]^{1/2}}\times\left[n(\omega_0)\Omega(E_\mathbf{k}+\hbar\omega_{\mathrm{LO}})\left[\frac{d\gamma}{dE_\mathbf{k}}\right]\Bigg|_{E_\mathbf{k}+\hbar\omega_{\mathrm{LO}}}+\{n(\omega_0)+1\}\Omega(E_\mathbf{k})\left[\frac{d\gamma}{dE_\mathbf{k}}\right]\Bigg|_{E_\mathbf{k}-\hbar\omega_{\mathrm{LO}}}\right], \tag{A4}$$

where

$$\Omega(E_\mathbf{k})=\ln\left[\frac{\gamma^{1/2}(E_\mathbf{k}-\hbar\omega_{\mathrm{LO}})+\gamma^{1/2}(E_\mathbf{k})}{|\gamma^{1/2}(E_\mathbf{k}-\hbar\omega_{\mathrm{LO}})-\gamma^{1/2}(E_\mathbf{k})|}\right] \tag{A5}$$

and

$$\gamma(E_\mathbf{k})=E_\mathbf{k}[1+\alpha E_\mathbf{k}+\beta E_\mathbf{k}^2]\ , \tag{A6}$$

where

$$\alpha=\frac{E_p^2}{E_g(E_g+E_p)^2} \tag{A7}$$

and

$$\beta=\frac{-2E_p^3}{E_g(E_g+E_p)^4}\ , \tag{A8}$$

where E_g is the band gap and E_p is given by

$$E_p=E_g\left[1+\frac{m_e}{m^*}\right], \tag{A9}$$

where m_e is the free-electron mass and m^* is the electron effective mass at the bottom of the Γ valley.

(b) Intravalley momentum relaxation

The momentum relaxation rate due to intravalley polar LO-phonon scattering in the Γ, L, and X bands was calculated assuming parabolic bands as[9]

$$\frac{1}{\tau_m}=\frac{e^2\omega_0 m^{*1/2}}{4\pi\epsilon_p\hbar(2E_\mathbf{k})^{1/2}}\left[n(\omega_0)\left\{\left[1+\frac{\hbar\omega_0}{E_\mathbf{k}}\right]^{1/2}-\frac{\hbar\omega_0}{E_\mathbf{k}}\sinh^{-1}\left[\frac{E_\mathbf{k}}{\hbar\omega_0}\right]^{1/2}\right\}+[n(\omega_0)+1]\left\{\left[1-\frac{\hbar\omega_0}{E_\mathbf{k}}\right]^{1/2}+\frac{\hbar\omega_0}{E_\mathbf{k}}\sinh^{-1}\left[\frac{E_\mathbf{k}}{\hbar\omega_0}-1\right]^{1/2}\right\}\right]. \tag{A10}$$

(c) Intervalley scattering rates

The scattering rate for equivalent and nonequivalent optical-phonon scattering to the L and X valleys was calculated assuming nonparabolicity:[11]

$$W(\mathbf{k})=\frac{D_{ij}^2 m_{jde}^{3/2}}{2^{1/2}\pi\hbar^3\rho\omega_{ij}}\frac{1}{e^{\hbar\omega_{ij}/k_BT}-1}\times\left[(E_\mathbf{k}-\Delta E_{ij}+\hbar\omega_{ij})^{1/2}+\exp\left[\frac{\hbar\omega_{ij}}{k_BT}\right](E_\mathbf{k}-\Delta E_{ij}-\hbar\omega_{ij})^{1/2}\right], \tag{A11}$$

where D_{ij} is the coupling constant between the ith and jth valleys, m_{jde} is the density-of-states effective mass in the jth valley, ΔE_{ij} is the difference in energy of the ith and jth valley minima, and ω_{ij} is the intervalley phonon frequency.

For scattering into the Γ valley, nonparabolicity was taken into account via[11]

$$W(\mathbf{k})=\frac{D_{ij}^2 m_\Gamma^{3/2}}{2^{1/2}\pi\hbar^3\rho\omega_{ij}}\frac{1}{e^{\hbar\omega_{ij}/k_BT}-1}\times[\gamma^{1/2}(E_\mathbf{k}+\hbar\omega_{ij})\gamma'(E_\mathbf{k}+\hbar\omega_{ij})+e^{\hbar\omega_{ij}/k_BT}\gamma^{1/2}(E_\mathbf{k}-\hbar\omega_{ij})\gamma'(E_\mathbf{k}-\hbar\omega_{ij})]\ . \tag{A12}$$

For intervalley scattering, the momentum relaxation rate $1/\tau_m$ is equal to the scattering rate $W(\mathbf{k})$.

(d) Acoustic-phonon scattering momentum relaxation

The acoustic-phonon momentum relaxation rate was calculated as[9]

$$\frac{1}{\tau_m}=\frac{2^{1/2}\Xi_{\mathrm{eff}}^2 m^{*3/2}k_BTE_\mathbf{k}^{1/2}}{\pi\hbar^4c_L}\ . \tag{A13}$$

(e) Alloy scattering momentum relaxation

The momentum relaxation rate for alloy scattering was calculated as[9]

$$W(\mathbf{k})=\frac{2\pi}{\hbar}(V_a-V_b)^2\Omega_0x(1-x)N(E_\mathbf{k})\ , \tag{A14}$$

where the alloy has the composition $A_xB_{1-x}C$ (here $\mathrm{Al}_x\mathrm{Ga}_{1-x}\mathrm{As}$), V_a and V_b are potentials associated with alloys AC and BC, respectively [here V_a-V_b is taken to be 0.3 eV (Ref. 12)], Ω_0 is the unit cell volume, and $N(E_\mathbf{k})$ is the conduction-band density of states at an energy $E_\mathbf{k}$ [Eq. (15)],

$$N(E_\mathbf{k})=\frac{(2m^*)^{3/2}E_\mathbf{k}^{1/2}}{4\pi^2\hbar^3}\ . \tag{A15}$$

2. Equations used in association with the potential distributions in this sample

The depletion zone width W, if $W < L_d$,

$$W = \left[\frac{2\epsilon_s V_{\text{rev}}}{eN_A} \right]^{1/2} \tag{A16}$$

and

$$\varepsilon_{\text{Fermi}} = \frac{eN_A(W-d)}{\epsilon_s} . \tag{A17}$$

Otherwise

$$W = L_d \tag{A18}$$

and

$$\varepsilon_{\text{Fermi}} = \frac{V_{\text{rev}}}{d} + \frac{eN_A L_d}{2\epsilon_s} - \frac{eN_A d}{\epsilon_s} . \tag{A19}$$

Generally, the effective field in the Γ valley[7]

$$\varepsilon_\Gamma = \varepsilon_{\text{Fermi}} - 1.50\times 10^{12} d , \tag{A20}$$

the effective field in the L valley[7]

$$\varepsilon_L = \varepsilon_{\text{Fermi}} - 1.28\times 10^{12} d , \tag{A21}$$

the effective field in the X valley[7]

$$\varepsilon_X = \varepsilon_{\text{Fermi}} - 2.50\times 10^{11} d + 5.72\times 10^{23} d^3 , \tag{A22}$$

the distance traveled in time Δt in the ith valley

$$\Delta d_i = \frac{p\Delta t}{m_i^*} + \frac{e\varepsilon_i(\Delta t)^2}{2m_i^*} , \tag{A23}$$

the momentum change in time Δt in the ith valley

$$\Delta p_i = e\varepsilon_i t , \tag{A24}$$

and the energy gained in time Δt in the ith valley

$$\Delta E_i = e\varepsilon_i \Delta d_i , \tag{A25}$$

where for the nonparabolic conduction-band mass $m_i^* = m^*_{\text{nonpara}}$ and is given by[9]

$$\frac{1}{m^*_{\text{nonpara}}} = \frac{1}{m^*_\Gamma} + \frac{3\alpha p^2}{(m^*_\Gamma)^2} , \tag{A26}$$

ϵ_s is the static dielectric constant, V_{rev} is the total reverse bias, e is electronic charge, N_A is the doping of the emitter layer, L_d is the thickness of the emitter layer, $\varepsilon_{\text{Fermi}}$ would be the electric field in a uniform alloy concentration emitter, ε_i (where $i = \Gamma$, L, or X) is the effective electric field in the ith minimum (this differs from $\varepsilon_{\text{Fermi}}$ due to the changing emitter layer composition), d is distance into the emitter layer from the surface, Δt is the time defined in the text, m^*_{nonpara} is the effective mass of an electron in the Γ valley including nonparabolicity effects, Δd_i is the distance traveled during time Δt in the ith minima, Δp_i is the momentum gained from the field during time Δt in the ith minima, ΔE_i is the energy gained from the field during time Δt in the ith minima, α is the constant defined in Eq. (A7) and m^*_Γ is the band-edge effective mass in the Γ valley.

---

[1] R. Mickevicius and A. Riklaitis, Semicond. Sci. Technol. **5**, 805 (1990).

[2] T. R. Parker, C. C. Phillips, and P. G. May (unpublished).

[3] R. L. Bell, *Negative Electron Affinity Devices* (Clarendon, Oxford, 1973).

[4] T. R. Parker, Ph.D. thesis, London University, 1994.

[5] J. R. Chelikowsky and M. L. Cohen, Phys. Rev. B **14**, 556 (1976).

[6] W. B. Wang, N. Ockman, M. A. Cavaccia, and R. R. Alfano, Appl. Phys. Lett. **57**, 395 (1990).

[7] S. Adachi, J. Appl. Phys. **58**, R1 (1985).

[8] J. G. Ruch and G. S. Kino, Appl. Phys. Lett. **10**, 40 (1967).

[9] B. K. Ridley, *Quantum Processes in Semiconductors* (Oxford University Press, Oxford, 1988).

[10] E. M. Conwell and M. O. Vassell, Phys. Rev. **166**, 2115 (1968).

[11] E. M. Conwell, *High Field Transport in Semiconductors,* Supplement to Solid State Physics (Academic, New York, 1967).

[12] A. K. Saxena, Phys. Rev. B **24**, 3295 (1981).